






Article

Mechanical Properties of Cubene Crystals

Leysan Kh. Galiakhmetova ^{1,†}, Igor S. Pavlov ^{2,†}, Ayrat M. Bayazitov ^{2,3,†}, Igor V. Kosarev ^{3,†}
and Sergey V. Dmitriev ^{2,3,*,†}

¹ Institute for Metals Superplasticity Problems of RAS, 450001 Ufa, Russia; rysaeva.l.h@gmail.com

² Mechanical Engineering Research Institute of the Russian Academy of Sciences—Branch of Federal Research Center “Institute of Applied Physics of RAS”, 603024 Nizhny Novgorod, Russia; ispavlov@mail.ru (I.S.P.); ayrseptember@mail.ru (A.M.B.)

³ Institute of Molecule and Crystal Physics, UFRC of RAS, 450075 Ufa, Russia; igork23v@mail.ru

* Correspondence: dmitriev.sergey.v@gmail.com

† These authors contributed equally to this work.

Abstract: The fullerene family, whose most popular members are the spherical C₆₀ and C₇₀ molecules, has recently added a new member, the cube-shaped carbon molecule C₈ called a cubene. A molecular crystal based on fullerenes is called fullerite. In this work, based on relaxational molecular dynamics, two fullerites based on cubenes are described for the first time, one of which belongs to the cubic system, and the other to the triclinic system. Potential energy per atom, elastic constants, and mechanical stress components are calculated as functions of lattice strain. It has been established that the cubic cubene crystal is metastable, while the triclinic crystal is presumably the crystalline phase in the ground state (the potential energies per atom for these two structures are −0.0452 and −0.0480 eV, respectively). The cubic phase has a lower density than the monoclinic one (volumes per cubene are 101 and 97.7 Å³). The elastic constants for the monoclinic phase are approximately 4% higher than those for the cubic phase. The presented results are the first step in studying the physical and mechanical properties of C₈ fullerite, which may have potential for hydrogen storage and other applications. In the future, the influence of temperature on the properties of cubenes will be analyzed.



Citation: Galiakhmetova, L.K.; Pavlov, I.S.; Bayazitov, A.M.; Kosarev, I.V.; Dmitriev, S.V.

Mechanical Properties of Cubene Crystals. *Materials* **2022**, *15*, 4871.
<https://doi.org/10.3390/ma15144871>

Academic Editor: Enrique Casarejos

Received: 9 June 2022

Accepted: 8 July 2022

Published: 13 July 2022

Publisher’s Note: MDPI stays neutral with regard to jurisdictional claims in published maps and institutional affiliations.



Copyright: © 2022 by the authors. Licensee MDPI, Basel, Switzerland. This article is an open access article distributed under the terms and conditions of the Creative Commons Attribution (CC BY) license (<https://creativecommons.org/licenses/by/4.0/>).

Keywords: cubene; elastic constants; equilibrium phases; fullerite; molecular dynamics

1. Introduction

The existence of large carbon molecules was predicted and described in some early papers, but a paper [1] published in 1985 caused an avalanche of publications on fullerenes. The smallest spherical fullerene is C₂₀; the most common molecules are C₆₀ and C₇₀, but fullerenes with a larger number of carbon atoms are easily obtained [2,3]. Probably the smallest possible carbon cluster is a cubic C₈ molecule called cubene [4].

Cubenes C₈ and cubanes C₈H₈ [5,6] are less studied than C₆₀ and C₇₀ fullerenes. The cubene molecule is highly strained, since a bond angle of 90° is energetically unfavorable; however, as follows from the ab initio study [7], the molecule should be stable because its energy corresponds to a deep minimum. Structural, electronic, and optical properties of cubane C₈H₈ and cubanoids (cubane-like molecules with hydrogen substituted by other atoms) were analyzed using a DFT approach [8].

Derivatives of cubane such as octanitrocubane and heptanitrocubane are excellent candidates for storage of large amounts of energy [9]. Thermochemical calculations show that 4145 kJ/mol is released during decomposition of the first, and 4346 kJ/mol of the second. Cuban can be used to obtain various bioisosteres, i.e., compounds obtained by replacing a group of atoms with a cubane, while maintaining the biological activity of the original compound. Thus, new substances with improved properties compared to the parent compound for pharmaceutical and agrochemical applications can be created [10]. Cubanes are also promising for hydrogen storage technologies [11–13].

Covalently bonded arrays of cubanes were shown to be possible [14]. Chemical modification of cubanes and cubane oligomers was analyzed in the work [15]. The electronic structure of C_8 and B_4N_4 cubic systems was analyzed [16]. It was shown that the functionalization of a chain of covalently bonded cubanes leads to a significant change in its conductivity [17,18]. This means that the electronic properties of cubane-based oligomers can be tuned by functionalization for applications in nanoelectronics.

Molecule crystals composed of fullerenes are called fullerites; they possess many promising physical, mechanical, and chemical properties for applications. Polymerization of fullerites under high pressure and temperature produces extremely hard materials with bulk modulus from 454 GPa to 644 GPa [19]. Fullerite demonstrates an anomalously slow thermal relaxation due to the excitation of internal vibrational degrees of freedom [20].

The mechanical properties of molecular crystals may differ from those of elemental solids, since the rotational degrees of freedom of molecules may play an important role [21–25]. There exist many examples of molecular crystals where rotations of molecules were analyzed [26–30]. Such crystals support rotobreathers that are dynamical regimes, in which one molecule (or particle) rotates, while others oscillate [31–35]. Properties of graphene can be described using particles with rotational degrees of freedom [36,37].

Metamaterials with particles having rotational degrees of freedom (polygons or polyhedrons) can be created artificially [38–42]. The rotational degrees of freedom can produce negative thermal expansion [21–25] or auxetic behaviour (negative Poisson's ratio) [38–42]. The crystal has been potentially used in several applications, such as bearing material for total hip implants [43].

The crystal structure of fullerites is of great importance, since the structure determines the properties of crystals. Fullerite C_{60} can be packed into a simple cubic or face-centered cubic (fcc) lattice [44,45]. In both lattices, a primitive translational cell contains one fullerene molecule. In the theoretical work [46], it was shown that, for C_{60} , the fcc structure is more stable than hexagonal close-packing (hcp), but for C_{70} hcp has lower energy than fcc lattice. The fcc structure of C_{60} at 0 K has an orthorhombic distortion due to ordering of fullerenes. At higher temperatures, there is a transition to an orientationally disordered fcc lattice [46]. As can be seen, many studies have been carried out to predict and analyze the structure of fullerites C_{60} and C_{70} , but we have not been able to find any information about the structure for fullerite C_8 except for the study [47] where cubic cubane C_8H_8 was described. In the present study, we set ourselves the task of finding the equilibrium phases of a cubane crystal and their mechanical properties.

2. Materials and Methods

Molecular dynamics is used to simulate the structure and mechanical properties of cubane crystals. Carbon–carbon interactions are described by the harmonic potential, while non-valence interactions are described by the Lennard–Jones potential. Each cubane interacts with the nearest, second and third neighboring cubanes. Below is a detailed description of the model.

A model of cubane molecule is shown in Figure 1. Each vertex of a cube with side ρ_0 contains a carbon atom. The covalent bonding of atoms in cubanes makes them relatively rigid. Cubanes interact with each other through much weaker van der Waals bonds.

In the present work, the equilibrium phases of a cubane crystal are described, and, in this case, cubane deformation plays an insignificant role. Therefore, covalent bonds are described by a simple harmonic potential. It is assumed that each carbon atom interacts through covalent bonds with the three nearest atoms and with the most distant atom, for example, atom 1 interacts with atoms 2, 4, 5, and 7 (see Figure 1). The interaction between the farthest neighbors is introduced to ensure the stability of the cubic shape of the molecule.

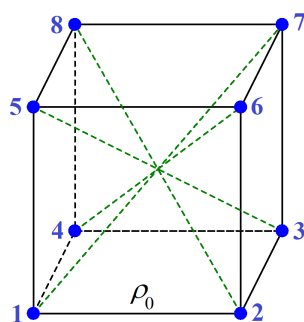


Figure 1. Cubene molecule model. Each vertex of a cube with side ρ_0 contains a carbon atom. Numbering of atoms in a cubene is shown. It is assumed that each carbon atom interacts through covalent bonds with the three nearest atoms and with the farthest atom; for example, atom 1 interacts with the atoms 2, 4, 5 and 7. Covalent bonds are described by the harmonic potential of stiffness K and equilibrium length ρ_0 for the nearest neighbors and $\sqrt{3}\rho_0$ for the farthest neighbors.

The equilibrium phases of cubene crystal are found using perturbative relaxational molecular dynamics. In this approach, the positions of the atoms are first perturbed to drive the system away from a local potential minimum, and then the structure is relaxed to reach a deeper energy minimum. Initially, cubenes with random orientation are arranged in the fcc lattice with periodic boundary conditions. The simulations are carried out for a computational cell that includes $2 \times 2 \times 2$ primitive translational cells of the fcc lattice. The total number of cubenes in the computational cell is $M = 8$, and the total number of carbon atoms is 64. The structure relaxation is performed with respect to the coordinates of the carbon atoms and with respect to the vectors specifying the periodic cell of the structure in order to achieve the state with zero forces acting on the atoms and zero external stresses applied to the computational cell.

Our model is built in the spirit of the work [20], where the deformation of valence bonds is described by the harmonic potential, and intermolecular interactions by the Lennard–Jones potential. Following this work, the potential energy of the cubene crystal described by the periodic computational cell with M cubenes can be written as follows:

$$P = \sum_{m=1}^M \sum_{n=1}^{12} U_n + \sum_{m=1}^M \sum_{k=1}^4 V_k + \sum_{i>j} \phi(|\mathbf{R}_{i,j}|). \quad (1)$$

The first term on the right-hand side of Equation (1) describes the valence interactions between nearest atoms in the cubenes; there are 12 nearest bonds in each cubene. The harmonic potential is used:

$$U_n = \frac{K}{2} (|r_n| - \rho_0)^2, \quad (2)$$

where $K = 31.77 \text{ eV}/\text{\AA}^2$ is the bond stiffness [48], $|r_n|$ is the distance between two nearest neighbors in a cubene molecule and $\rho_0 = 1.418 \text{ \AA}$ is the equilibrium bond length. From Figure 1, it can be seen that the twelve bonds between nearest neighbors connect the following pairs of atoms: 1-2, 2-3, 3-4, 4-1, 1-5, 2-6, 3-7, 4-8, 5-6, 6-7, 7-8 and 8-5.

The second term on the right-hand side of Equation (1) describes the valence interactions between farthest atoms in the cubenes; there are four longest bonds in each cubene; they are described by the harmonic potential:

$$V_k = \frac{K}{2} (|r_k| - \sqrt{3}\rho_0)^2, \quad (3)$$

where K is the bond stiffness the same as for the bonds between nearest atoms, $|r_k|$ is the distance between two farthest neighbors in a cubene molecule and $\sqrt{3}\rho_0 = 2.456 \text{ \AA}$ is the

equilibrium bond length. From Figure 1, it can be seen that the four bonds between farthest neighbors connect the following pairs of atoms: 1-7, 2-8, 3-5 and 4-6.

The third term on the right-hand side of Equation (1) describes the van der Waals interactions between carbon atoms of different cubenes. The computational cell includes $8M$ atoms numbered by the index $i = 1, 2, \dots, 8M$. The i -th atom has the radius vector $\mathbf{r}_i = (r_{i,x}, r_{i,y}, r_{i,z})$, and $\mathbf{R}_{i,j} = \mathbf{r}_j - \mathbf{r}_i$. The van der Waals interactions are described by the Lennard–Jones potential

$$\phi(\xi) = 4\epsilon \left[\left(\frac{\sigma}{\xi} \right)^{12} - \left(\frac{\sigma}{\xi} \right)^6 \right], \quad (4)$$

where $\epsilon = 0.002757$ eV and $\sigma = 3.393$ Å [49]. The van der Waals interactions are taken into account with the cut-off radius so that each cubene interacts with 12 nearest, 6 next-nearest, and 24 next-next-nearest cubenes. Van der Waals interactions between atoms belonging to the same cubene are not taken into account.

A comment should be made on the choice of interatomic potentials used in this work. To date, a number of interatomic potentials have been developed for carbon materials, the most popular of which are REBO-I [50], REBO-II [51], C-EDIP [52], Tersoff [53], LCBOPI [54], ReaxFFC-2013 [55] and AIREBO [56] potentials and recently developed machine-learning potential GAP-20 [57]. Each potential has been designed for specific purposes. In this study, we do not consider high pressures or temperatures, so the potential can be greatly simplified to speed up the simulation. The van der Waals bonds describing the interaction between cubenes are two orders of magnitude weaker than covalent bonds within a cubene. Therefore, for our study for covalent bonds, the simplest harmonic potential is sufficient.

A home-made code written in the C++ algorithmic language is developed for simulations. Components of the stress tensor σ_{ij} are calculated as described, e.g., in [58]. The gradient method is used to minimize the potential energy of the crystal Equation (1) with respect to the coordinates of carbon atoms and with respect to the translation vectors of the computational cell. The relaxation is complete when the maximal force acting on atoms does not exceed 10^{-9} eV/Å and the value of the maximal stress component does not exceed 10^{-6} eV/Å³.

For the relaxed structure, the potential energy per atom and the elastic constants C_{ij} are calculated as described, for example, in [58]. By doing so, the elastic constants in Hooke's law

$$\begin{bmatrix} \sigma_{xx} \\ \sigma_{yy} \\ \sigma_{zz} \\ \sigma_{xy} \\ \sigma_{xz} \\ \sigma_{yz} \end{bmatrix} = \begin{bmatrix} C_{11} & C_{12} & C_{13} & C_{14} & C_{15} & C_{16} \\ C_{21} & C_{22} & C_{23} & C_{24} & C_{25} & C_{26} \\ C_{31} & C_{32} & C_{33} & C_{34} & C_{35} & C_{36} \\ C_{41} & C_{42} & C_{43} & C_{44} & C_{45} & C_{46} \\ C_{51} & C_{52} & C_{53} & C_{54} & C_{55} & C_{56} \\ C_{61} & C_{62} & C_{63} & C_{64} & C_{65} & C_{66} \end{bmatrix} \begin{bmatrix} \varepsilon_{xx} \\ \varepsilon_{yy} \\ \varepsilon_{zz} \\ \varepsilon_{xy} \\ \varepsilon_{xz} \\ \varepsilon_{yz} \end{bmatrix}, \quad (5)$$

are determined. Note that, for any crystal, $C_{ij} = C_{ji}$ and, consequently, the maximum number of elastic constants is 21, although there are fewer of them for crystals with high symmetry.

We also calculate the potential energy, stress components, and elastic constants of the cubene crystal as the functions of homogeneous strain. After applying the homogeneous deformation, the structure is relaxed with respect to atomic displacements in order to achieve practically zero forces acting on the atoms. Stress components and elastic constants are calculated for relaxed structure. Briefly, the research flow can be described as follows. First, equilibrium phases are found, then the stability of the phases with respect to uniform deformation is analyzed, and then properties of the phases, such as energy, stress–strain curves, and elastic constants, are calculated.

3. Results

Let us present the numerical results obtained for cubene crystals. First, two equilibrium phases will be described. Then, the stability of the phases with respect to uniform elastic deformation will be demonstrated. Finally, elastic constants and stress–strain curves will be presented for both equilibrium phases.

3.1. Two Equilibrium Phases

The structure relaxation was carried out for 50 initial configurations with randomly oriented cubenes having centers of gravity at the sites of the fcc lattice with the distance between nearest neighbors equal to 5.3 Å. In many cases, metastable structures with a relatively high potential energy have been obtained. In some cases, two equilibrium phases with a relatively low potential energy were found. One of them has cubic symmetry, and the other belongs to the triclinic system. These two phases are described below.

The structure of the crystal will be defined by the translation vectors of the primitive cell, \mathbf{a} , \mathbf{b} , \mathbf{c} , and coordinates of the carbon atoms in the cell, ζ_i . Then, the radius-vector of any atom in the crystal can be expressed as follows:

$$\mathbf{r}_{\alpha\beta\gamma i} = \alpha\mathbf{a} + \beta\mathbf{b} + \gamma\mathbf{c} + \zeta_i, \quad (6)$$

where α , β , and γ are arbitrary integers.

3.1.1. Metastable Cubic Phase

A primitive translation cell of cubic phase includes two cubenes, see Figure 2. Translation vectors of a primitive cell for the cubic phase are

$$\mathbf{a} = (\delta, 0, 0), \quad \mathbf{b} = (\delta, \delta, 0), \quad \mathbf{c} = (\delta/2, 0, \delta/2), \quad (7)$$

where $\delta = 7.39223$ Å. The translation vectors have lengths (in angstrom)

$$|\mathbf{a}| = \delta = 7.392, \quad |\mathbf{b}| = \sqrt{2}\delta = 10.454, \quad |\mathbf{c}| = \delta/\sqrt{2} = 5.227. \quad (8)$$

The angles between translation vectors are

$$\widehat{\mathbf{a}, \mathbf{b}} = 0.7854 = 45^\circ, \quad \widehat{\mathbf{a}, \mathbf{c}} = 0.7854 = 45^\circ, \quad \widehat{\mathbf{b}, \mathbf{c}} = 1.0472 = 60^\circ. \quad (9)$$

Volume per one cubene is 101.00 Å³.

Coordinates of 16 carbon atoms in a primitive translation cell are (in angstrom):

1-st cubene:

$$\begin{aligned} \zeta_1 &= (1.41966, 0.00162041, 1.4202), \\ \zeta_2 &= (1.89262, 0.941731, 0.470774), \\ \zeta_3 &= (0.942768, 0.469339, -0.469764), \\ \zeta_4 &= (0.470234, -0.471199, 0.480089), \\ \zeta_5 &= (0.479549, 0.951046, 1.89302), \\ \zeta_6 &= (0.952083, 1.89158, 0.943166), \\ \zeta_7 &= (0.0026573, 1.41876, 0.0030558), \\ \zeta_8 &= (-0.470304, 0.478654, 0.952482). \end{aligned}$$

2-nd cubene:

$$\begin{aligned} \zeta_9 &= (5.11614, 5.11488, 0.00305583), \\ \zeta_{10} &= (4.16686, 5.5877, 0.943167), \\ \zeta_{11} &= (3.22632, 4.63785, 0.470774), \\ \zeta_{12} &= (4.17603, 4.16545, -0.469764), \\ \zeta_{13} &= (5.58896, 4.17477, 0.952481), \\ \zeta_{14} &= (4.63925, 4.64716, 1.89302), \\ \zeta_{15} &= (3.69914, 3.69774, 1.4202), \\ \zeta_{16} &= (4.64843, 3.22492, 0.480089). \end{aligned}$$

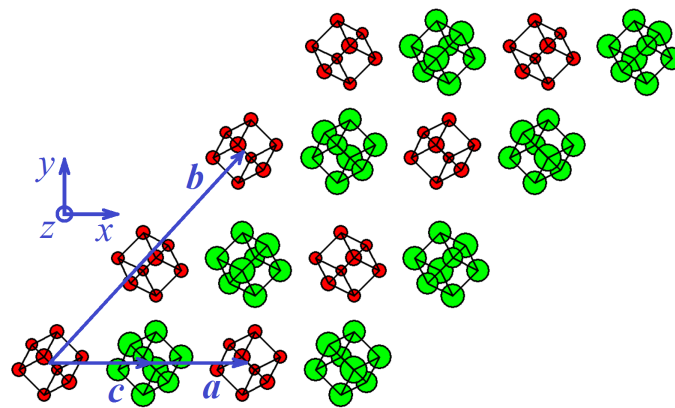


Figure 2. Structure of cubic cubene. The larger the z coordinate, the larger circle shows the carbon atom. Red (green) color is used for the lower (upper) plane of the structure (only two planes of cubenes are shown). The centers of gravity of the cubenes are close to the points of the fcc lattice. Vectors of the primitive translation cell, a , b , and c , are given by Equation (7). A primitive translational cell includes two cubenes differently oriented in space.

3.1.2. Stable Triclinic Phase

A primitive translation cell of triclinic phase includes one cubene, see Figure 3. Translation vectors of a primitive cell for the triclinic phase are (in angstrom)

$$\mathbf{a} = (7.34266, 0, 0), \quad \mathbf{b} = (3.34246, 3.65657, 0), \quad \mathbf{c} = (4.00020, 0.359778, 3.63883). \quad (10)$$

The translation vectors have lengths (in angstrom)

$$|\mathbf{a}| = 7.343, \quad |\mathbf{b}| = 4.954, \quad |\mathbf{c}| = 5.420. \quad (11)$$

The angles between translation vectors are

$$\widehat{\mathbf{a}, \mathbf{b}} = 0.8302 = 47.57^\circ, \quad \widehat{\mathbf{a}, \mathbf{c}} = 0.7405 = 42.43^\circ, \quad \widehat{\mathbf{b}, \mathbf{c}} = 0.9920 = 56.84^\circ. \quad (12)$$

The volume per cubene is 97.70 \AA^3 , which is less than that of the cubic phase and, therefore, the triclinic phase is denser.

Coordinates of eight carbon atoms in a primitive translation cell are (in angstrom):

$$\begin{aligned} \xi_1 &= (0.985844, -0.408445, 0.510329), \\ \xi_2 &= (1.907106, 0.599395, 0.891091), \\ \xi_3 &= (1.348457, 1.474166, -0.074438), \\ \xi_4 &= (0.427158, 0.466286, -0.455156), \\ \xi_5 &= (0.064547, 0.069598, 1.475858), \\ \xi_6 &= (0.985846, 1.077477, 1.856576), \\ \xi_7 &= (0.427160, 1.952208, 0.891091), \\ \xi_8 &= (-0.494102, 0.944369, 0.510329). \end{aligned}$$

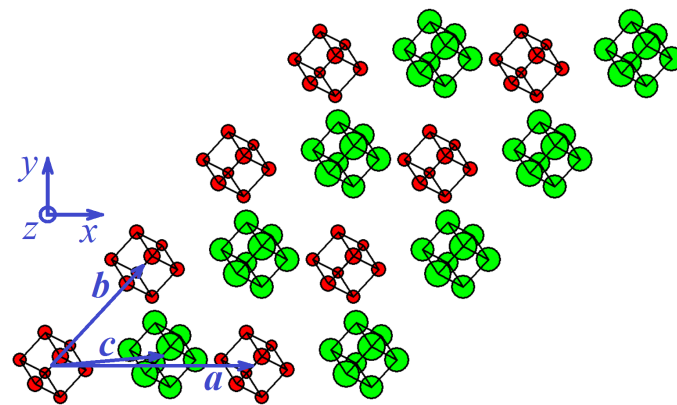


Figure 3. Structure of triclinic cubene. The larger the z coordinate, the larger circle shows the carbon atom. Red (green) color is used for the lower (upper) plane of the structure (only two planes of cubenes are shown). Vectors of the primitive translation cell, a , b , and c , are given by Equation (10). A primitive translational cell includes one cubene; therefore, all cubenes have the same orientation in space.

3.2. Energy of Cubic and Triclinic Cubene Crystals

Potential energy per atom for equilibrium cubic cubene is -0.045185 eV and, for equilibrium triclinic cubene, it is lower and equal to -0.047987 eV. The triclinic phase has the lowest energy among all structures obtained by relaxation of randomly oriented cubenes. We assume that the triclinic cubene crystal has the lowest possible energy, but we cannot provide a rigorous proof of this fact.

It is important to demonstrate that the crystals are stable with respect to application of elastic strain. The potential energy per atom was calculated for various values of the strain component ε_{ij} , while all other strain components were equal to zero. The results are plotted in Figure 4 for (a) cubic and (b) triclinic crystals. Note that the application of any strain component, positive or negative, leads to an increase in the potential energy of the crystal. This means that cubic and triclinic crystals are structurally stable up to $\pm 5\%$ strain.

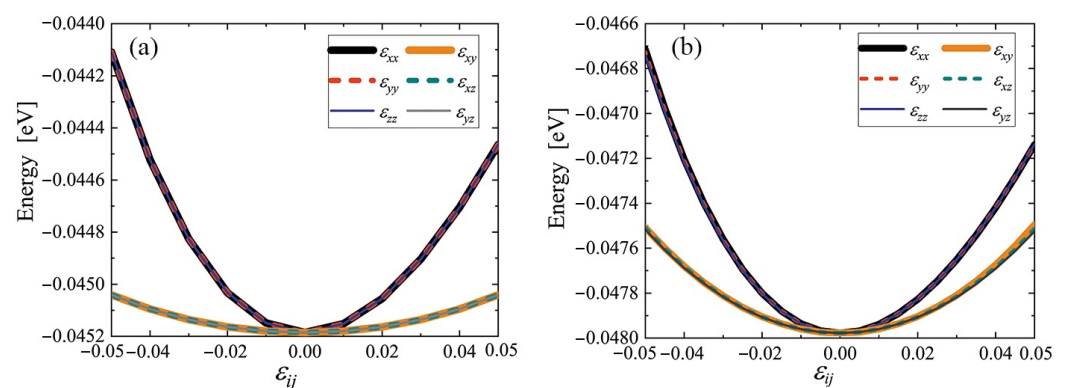


Figure 4. Potential energy per atom of cubic (a) and triclinic (b) cubene crystals depending on strain ε_{ij} . Only one component of the strain tensor is varied, the rest are equal to zero.

For a cubic crystal, the curves for the normal strain components ε_{xx} , ε_{yy} , and ε_{zz} in Figure 4a coincide, the same is true for the shear strains ε_{xy} , ε_{xz} , and ε_{yz} . This fact reflects the lattice symmetry.

For the low-symmetry triclinic phase, the curves in Figure 4b do not match, but the difference is small for normal and shear strains. It can be concluded that the triclinic phase is weakly anisotropic.

3.3. Elastic Constants for the Cubene Crystals

The stress components are related to the strain components according to Hooke's law Equation (5), which for the cubic crystal assumes the form (elastic constants are given in GPa)

$$\begin{bmatrix} \sigma_{xx} \\ \sigma_{yy} \\ \sigma_{zz} \\ \sigma_{xy} \\ \sigma_{xz} \\ \sigma_{yz} \end{bmatrix} = \begin{bmatrix} 464.5 & 177.1 & 177.1 & 0 & 0 & 0 \\ 177.1 & 464.5 & 177.1 & 0 & 0 & 0 \\ 177.1 & 177.1 & 464.5 & 0 & 0 & 0 \\ 0 & 0 & 0 & 177.1 & 0 & 0 \\ 0 & 0 & 0 & 0 & 177.1 & 0 \\ 0 & 0 & 0 & 0 & 0 & 177.1 \end{bmatrix} \begin{bmatrix} \varepsilon_{xx} \\ \varepsilon_{yy} \\ \varepsilon_{zz} \\ \varepsilon_{xy} \\ \varepsilon_{xz} \\ \varepsilon_{yz} \end{bmatrix}. \quad (13)$$

It is well known that isotropic elastic media are characterized by two independent elastic constants, while crystals with cubic symmetry generally have three independent elastic constants [59–62]. There are only two independent elastic constants in Hooke's law Equation (13), since pairwise interatomic potentials are used, and the Cauchy relation is satisfied, which imposes an additional restriction on elastic constants [63].

For the triclinic cubene crystal, the Hooke's law reads (elastic constants are given in GPa)

$$\begin{bmatrix} \sigma_{xx} \\ \sigma_{yy} \\ \sigma_{zz} \\ \sigma_{xy} \\ \sigma_{xz} \\ \sigma_{yz} \end{bmatrix} = \begin{bmatrix} 477.0 & 187.0 & 183.8 & 9.0 & -9.9 & 16.2 \\ 187.0 & 481.6 & 179.1 & 16.4 & 20.1 & -5.0 \\ 183.8 & 179.1 & 484.6 & -26.0 & -9.6 & -10.5 \\ 9.0 & 16.4 & -26.0 & 187.0 & 16.2 & 20.1 \\ -9.9 & 20.1 & -9.6 & 16.2 & 183.8 & -26.0 \\ 16.2 & -5.0 & -10.5 & 20.1 & -26.0 & 179.1 \end{bmatrix} \begin{bmatrix} \varepsilon_{xx} \\ \varepsilon_{yy} \\ \varepsilon_{zz} \\ \varepsilon_{xy} \\ \varepsilon_{xz} \\ \varepsilon_{yz} \end{bmatrix}. \quad (14)$$

In Equation (14), due to the Cauchy relations, one has $C_{44} = C_{12}$, $C_{55} = C_{13}$, and $C_{66} = C_{23}$. Analysis of the elastic constants confirms that the triclinic cubene crystal is weakly anisotropic. The constants C_{11} , C_{22} , and C_{33} differ by no more than 1.6%. The constants C_{44} , C_{55} , and C_{66} differ by no more than 4.2%.

A comparison of the elastic constants of the cubic and triclinic cubenes indicates that the latter is stiffer. Indeed, in Equation (13), $C_{11} = C_{22} = C_{33} = 464.5$ GPa, and, in Equation (14), these elastic constants are higher. The same applies to the shear moduli, which, for a cubic crystal are $C_{44} = C_{55} = C_{66} = 177.1$ GPa, which is less than for a triclinic crystal. The higher stiffness of the triclinic crystal is due to its greater density.

3.4. Stress–Strain Curves

The stress–strain curves for cubic and triclinic cubene crystals are presented in Figures 5 and 6, respectively. For the abscissa, the only nonzero strain component is used, and the other strain components are zero. The normal stress components are shown by black (σ_{xx}), red (σ_{yy}), and blue (σ_{zz}) lines. The shear stresses are plotted by yellow (σ_{xy}), cyan (σ_{xz}), and gray (σ_{yz}) lines. In some cases, dashed lines are used to show overlapping curves.

As can be seen from Figures 5 and 6, when normal strain is applied, the shear stresses are equal to zero in cubic crystal, but, in the triclinic crystal, they are not.

For the normal stress components, as the functions of the normal strain components [panels (a) to (c) in Figures 5 and 6] within the studied strain range $\pm 5\%$ demonstrate, there is a noticeable deviation from the linear dependence. On the other hand, the stress–strain curves $\sigma_{ij}(\varepsilon_{ij})$ for $i \neq j$ show a linear relationship in this strain range (see panels (d) to (f) in Figures 5 and 6).

The elastic constants C_{11} , C_{22} , and C_{33} as the functions of strain are plotted in Figures 7 and 8 for cubic and triclinic cubene crystals, respectively. In the studied strain range $\pm 5\%$, these elastic constants depend almost linearly on the normal strain components and weakly depend on the shear strain components.

The elastic constants C_{44} , C_{55} , and C_{66} as the functions of strain are plotted in Figures 9 and 10 for cubic and triclinic cubene crystals, respectively. In the studied strain range $\pm 5\%$, these elastic

constants depend almost linearly on the normal strain components and weakly depend on the shear strain components.

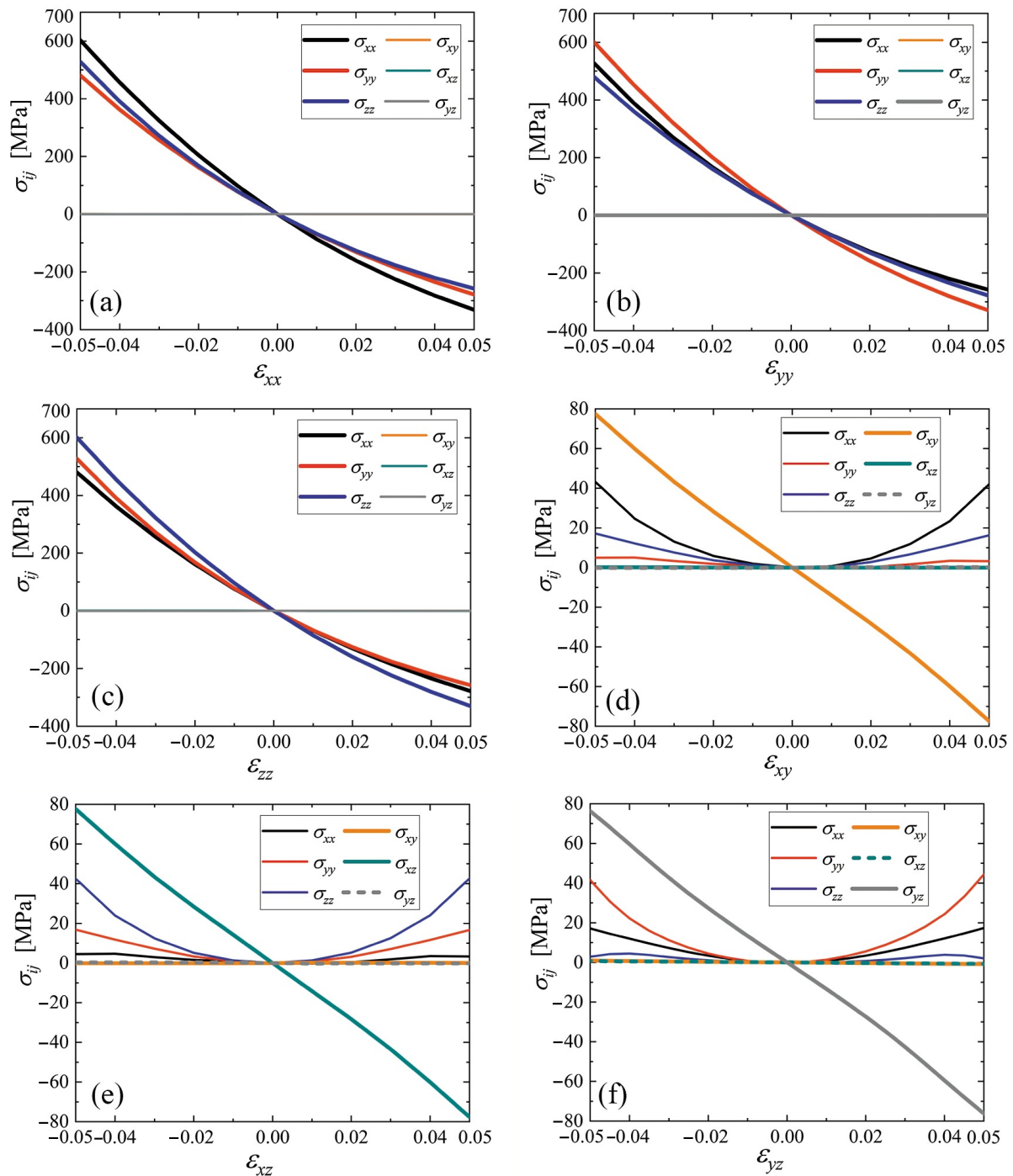


Figure 5. Stress–strain curves for cubic cubene crystal. Only one component of the strain tensor is varied, and the rest are equal to zero. The normal stress components are shown by black (σ_{xx}), red (σ_{yy}), and blue (σ_{zz}) lines. The shear stresses are plotted by yellow (σ_{xy}), cyan (σ_{xz}), and gray (σ_{yz}) lines. In some cases, dashed lines are used to show overlapping curves. Panels (a–f) correspond to changing ϵ_{xx} to ϵ_{yz} , respectively.

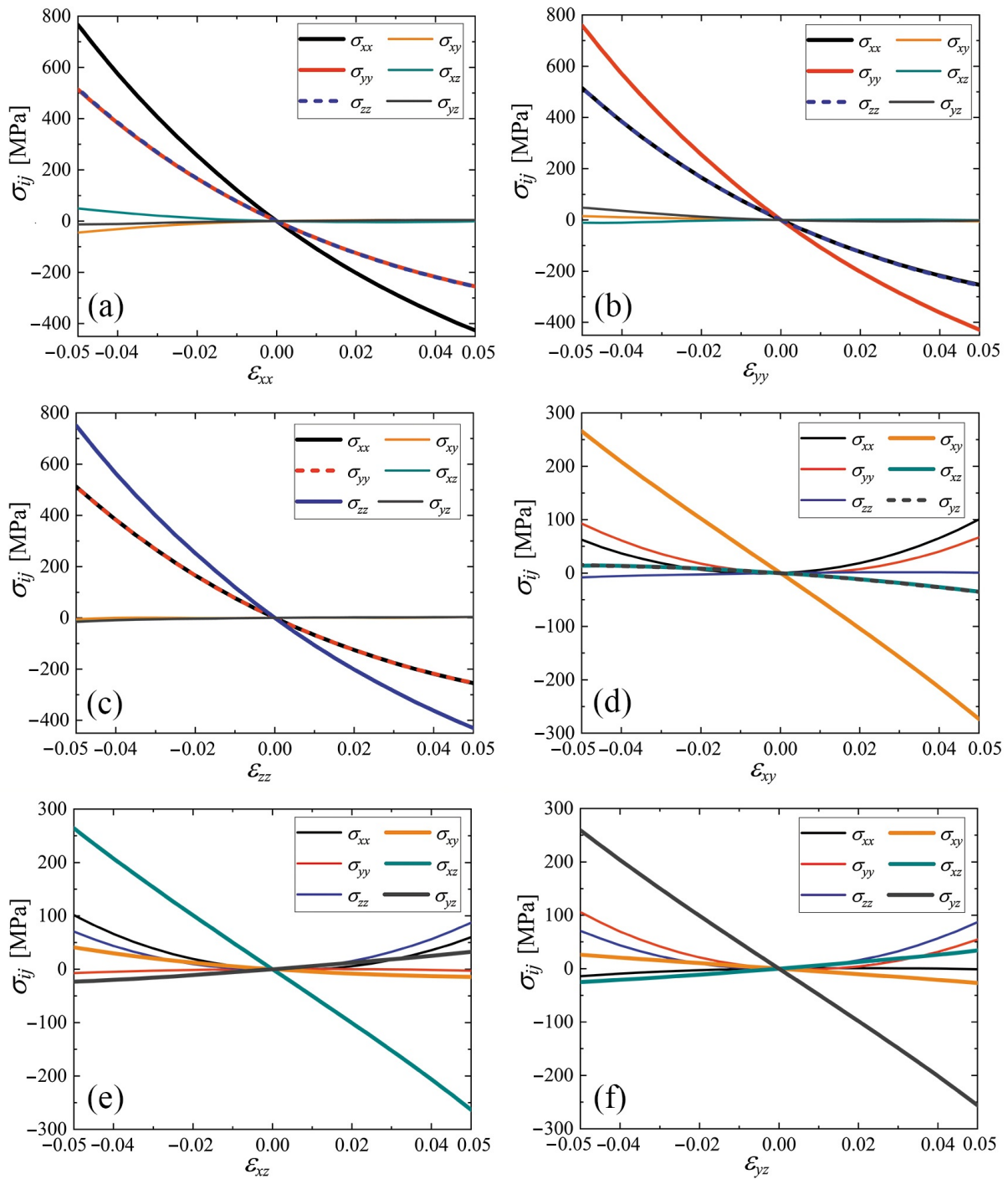


Figure 6. Stress–strain curves for triclinic cubene crystal. Only one component of the strain tensor is varied, the rest are equal to zero. Line colors are the same as in Figure 5. Panels (a–f) correspond to changing ϵ_{xx} to ϵ_{yz} , respectively.

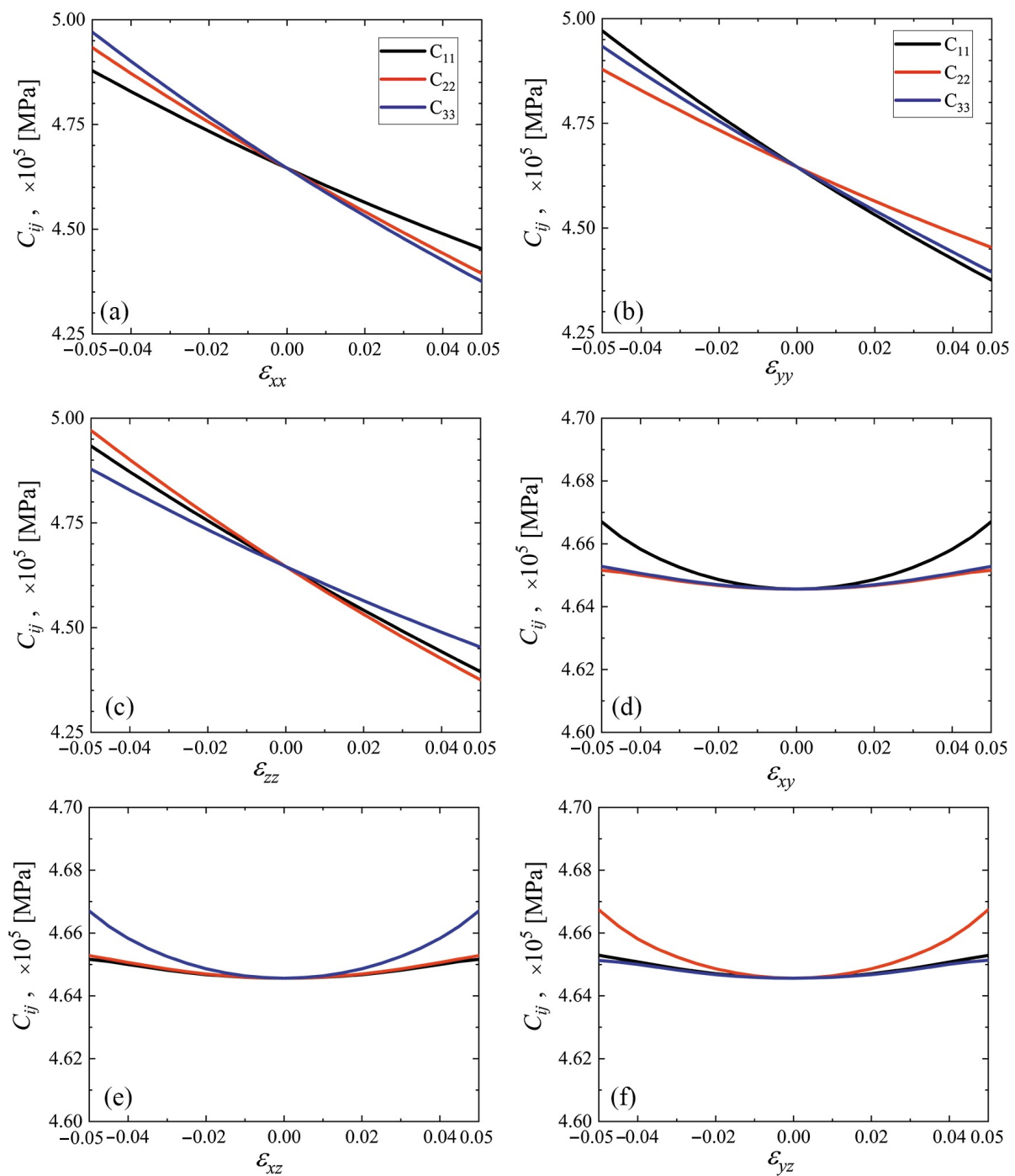


Figure 7. Elastic constants C_{11} , C_{22} , and C_{33} as the functions of strain for cubic cubene crystal (black, red, and blue lines, respectively). Only one component of the strain tensor is varied, the rest are equal to zero. Panels (a–f) correspond to changing ϵ_{xx} to ϵ_{yz} , respectively.

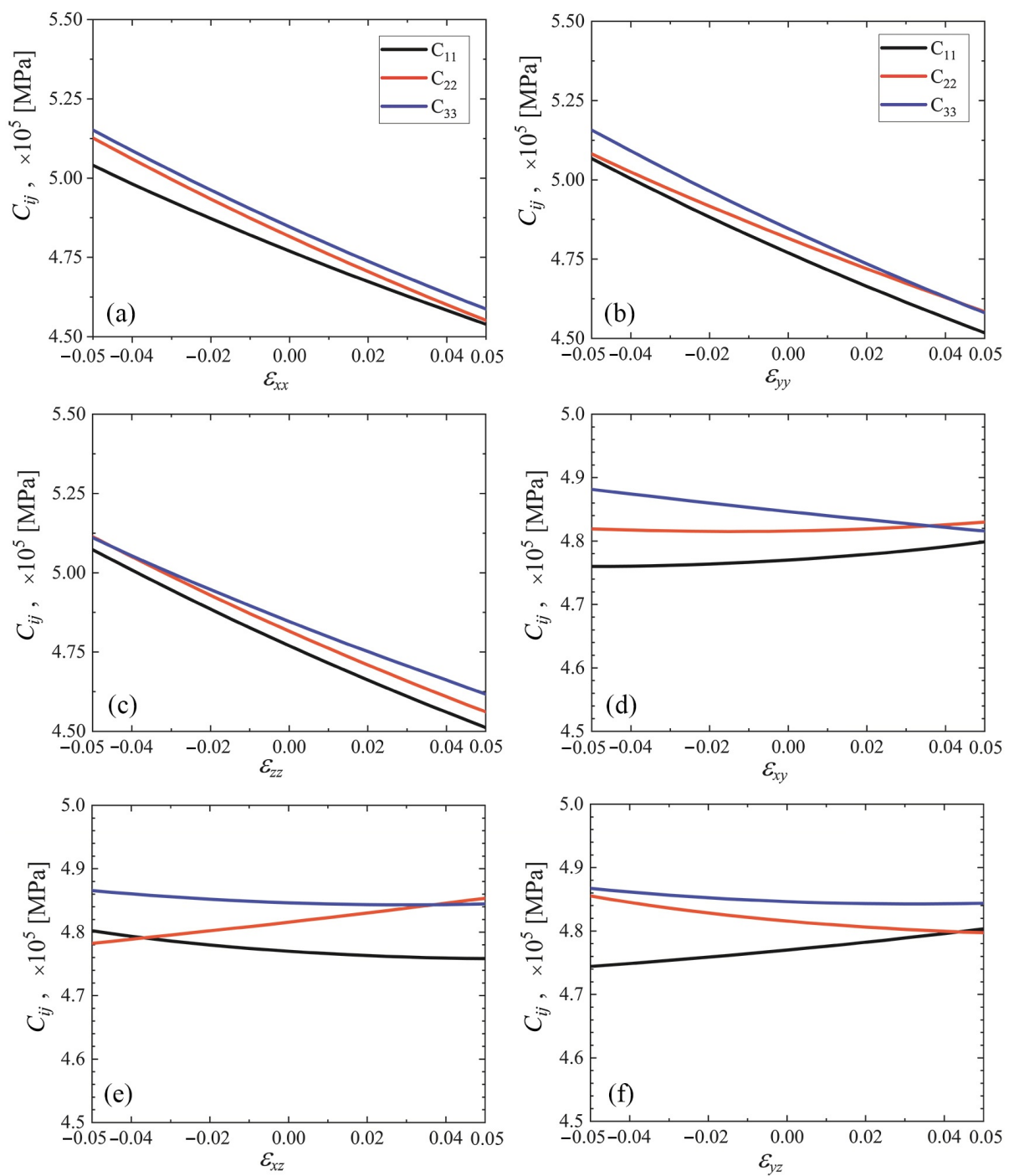


Figure 8. The same as in Figure 7, but for the triclinic crystal. Panels (a–f) correspond to changing ϵ_{xx} to ϵ_{yz} , respectively.

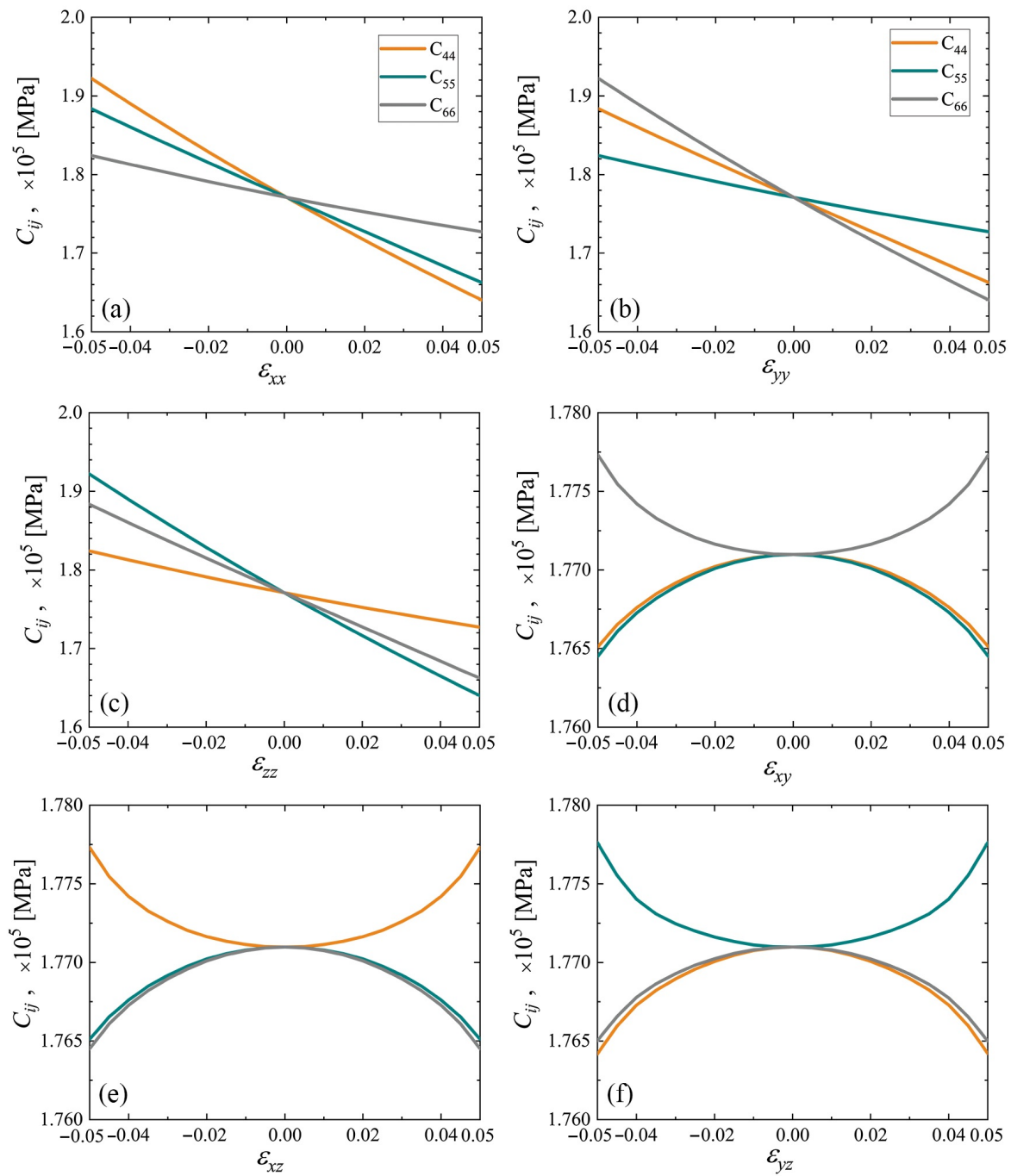


Figure 9. Elastic constants C_{44} , C_{55} , and C_{66} as the functions of strain for cubic cubene crystal (yellow, cyan, and gray lines, respectively). Only one component of the strain tensor is varied, the rest are equal to zero. Panels (a–f) correspond to changing ϵ_{xx} to ϵ_{yz} , respectively.

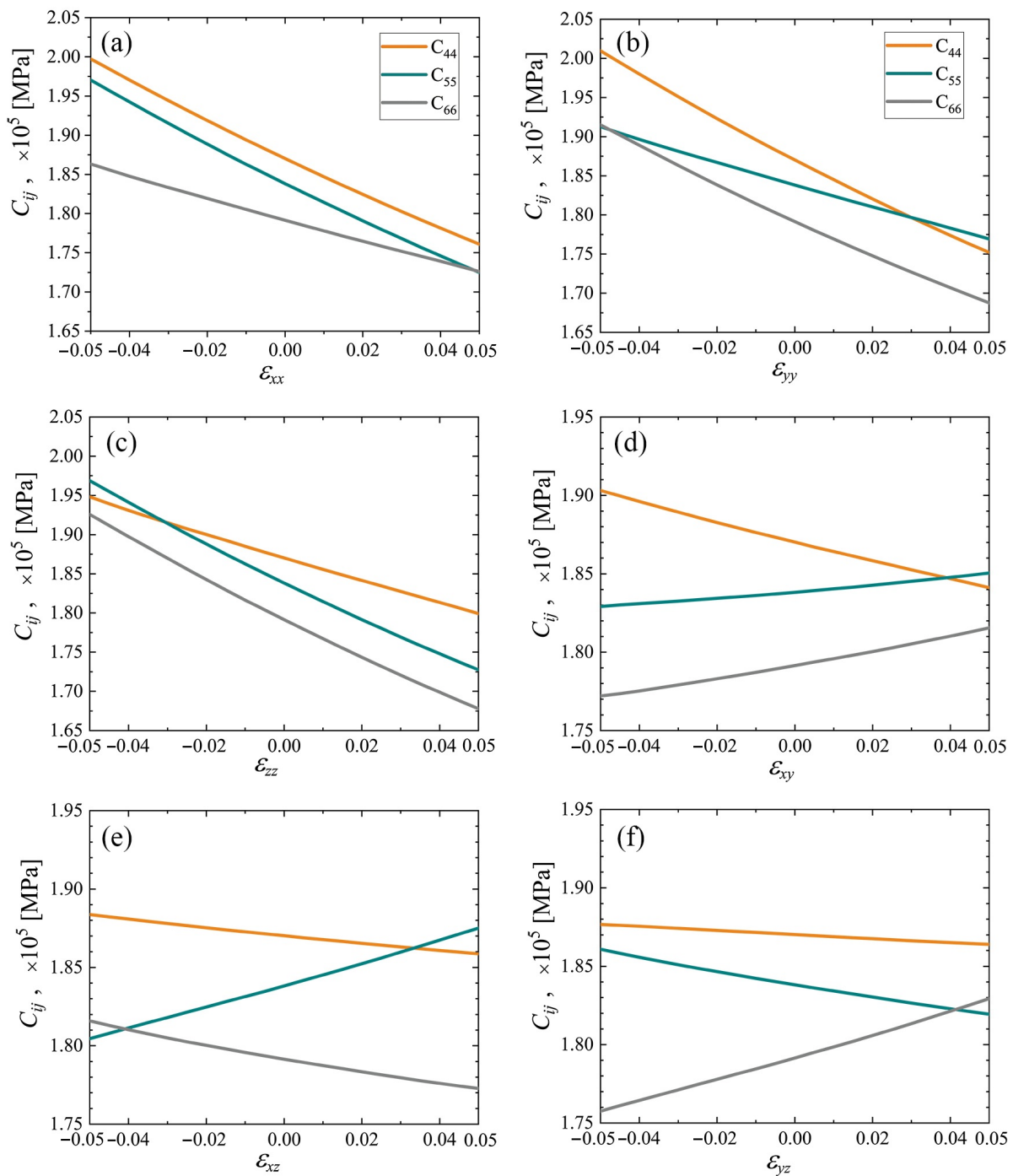


Figure 10. The same as in Figure 9, but for the triclinic crystal. Panels (a–f) correspond to changing ε_{xx} to ε_{yz} , respectively.

4. Discussion

Two equilibrium phases of the C_8 molecular crystal were found for the first time based on perturbative relaxation molecular dynamics simulations. The phase of cubic symmetry is metastable with a sublimation energy of -0.045 eV per atom. A primitive translational cell of a cubic cubene contains two cubenes with the volume of 101 \AA^3 per one cubene, see Figure 2. A triclinic cubene has a sublimation energy of -0.048 eV per atom, its primitive translational cell includes one cubene, and each cubene occupies a volume of 97.7 \AA^3 , see Figure 3. The triclinic phase is most likely the ground state of the cubene crystal.

Stress–strain curves for cubic and triclinic cubenes were calculated in the strain range $\pm 5\%$, see Figures 5 and 6, respectively. No phase transformations were observed in this strain range; therefore, both phases in this strain range are structurally stable. Components of normal stress in the strain range $\pm 5\%$ show noticeable deviation from the linear Hooke's law.

The elastic constants C_{11} , C_{22} , and C_{33} as the functions of strain for cubic and triclinic cubene crystals are presented in Figures 7 and 8, respectively. Shear moduli C_{44} , C_{55} , and C_{66} depending on strain for cubic and triclinic cubene crystals are shown in Figures 9 and 10, respectively. Elastic constants C_{11} , C_{22} , and C_{33} depend almost linearly on strain, while constants C_{44} , C_{55} , and C_{66} are weakly dependent on strain.

Elastic properties of cubenes can be compared to that of fullerenes. Young's modulus of the fcc single crystal fullerite C_{60} at room temperature was measured in [64] to be 20 ± 5 GPa. For C_{60} fullerene nanowires, the Young's modulus is 15.1 ± 1.39 [65], while, in bcc tetragonal C_{60} nanowire, it is 30 GPa [66]. According to our calculations, stiffness of cubenes is one order of magnitude higher, see Equations (13) and (14). This difference is related to the small size of C_8 cubenes, which greatly increases the number of van der Waals bonds per atom. In addition, note that our calculations are made for zero temperature and, as is well known, the rigidity of molecular crystals decreases very rapidly with increasing temperature [64].

The limitations of our study are as follows. Since the harmonic potential is used to describe covalent bonds, high pressure and the possible transformation of the structure due to polymerization cannot be modeled within our model. The influence of temperature was not taken into account and, consequently, the range of thermal stability of the obtained structures was not established.

5. Conclusions and Future Work

Two equilibrium phases of C_8 fullerite crystal were discovered by the relaxational molecular dynamics method, one of which has cubic and the other triclinic symmetry, see Figures 2 and 3, respectively. The energy per atom for the triclinic phase is 0.0028 eV lower than that for the cubic phase, and triclinic fullerite is presumably the ground state structure. Both phases are stable with respect to uniform strain $\pm 5\%$, see Figure 4. The stability of structures with respect to thermal vibrations was not analyzed in this work.

Stress–strain curves for cubic and triclinic fullerite demonstrate noticeable nonlinearity in the range of uniform normal strain $\pm 5\%$, see panels (a)–(c) in Figures 5 and 6. On the other hand, stress–strain curves for shear strain are almost linear, see panels (d)–(f) in Figures 5 and 6.

The elastic constants C_{11} , C_{22} , and C_{33} as the functions of strain are presented in Figures 7 and 8 for cubic and triclinic cubenes, respectively. Similar results for shear moduli C_{44} , C_{55} , and C_{66} can be seen in Figures 9 and 10 for cubic and triclinic cubenes, respectively. Elastic constants C_{11} , C_{22} , and C_{33} vary almost linearly with strain, while constants C_{44} , C_{55} , and C_{66} are weakly dependent on strain.

The results presented here are the first step in studying the physical properties of cubenes. Future studies will analyze phonon dispersion curves, nonlinear dynamics of cubenes including rotobreathers [31–35], and crowdions [67]. To solve these problems, a more complex interatomic potential should be used [50–57]. The effect of temperature on the mechanical properties and thermal expansion will be analyzed. Another interesting line of future research is the development of continuum models capable of describing the vibrational spectra of cubenes. We hope that our study will stimulate experimental work on the mechanical and physical properties of cubenes. In particular, it would be of interest to analyze the polymerization of cubenes during high-temperature treatment under high pressure, similar to what was done in [68] for C_{60} and C_{70} fullerenes.

Author Contributions: Conceptualization, S.V.D. and I.S.P.; methodology, I.S.P.; software, I.V.K.; investigation, L.K.G. and A.M.B.; writing—original draft preparation, S.V.D.; writing—review and editing, S.V.D. and I.S.P. All authors have read and agreed to the published version of the manuscript.

Funding: For I.S.P, A.M.B., and S.V.D., this research was funded by the Russian Science Foundation, Grant No. 21-19-00813.

Informed Consent Statement: Not applicable.

Data Availability Statement: The data of this study are available from the corresponding author upon reasonable request.

Conflicts of Interest: The authors declare no conflict of interest.

References

1. Kroto, H.W.; Heath, J.R.; O'Brien, S.C.; Curl, R.F.; Smalley, R.E. C₆₀: Buckminsterfullerene. *Nature* **1985**, *318*, 162–163. [[CrossRef](#)]
2. Kawada, H.; Fujii, Y.; Nakao, H.; Murakami, Y.; Watanuki, T.; Suematsu, H.; Kikuchi, K.; Achiba, Y.; Ikemoto, I. Structural aspects of C₈₂ and C₇₆ crystals studied by x-ray diffraction. *Phys. Rev. B* **1995**, *51*, 8723–8730. [[CrossRef](#)] [[PubMed](#)]
3. Bubenchikov, M.; Mamontov, D.; Azheev, A.; Azheev, S. Study of the influence of the Dzhanibekov effect on the dynamic state of fullerene C₁₀₀. *J. Phys. Conf. Ser.* **2022**, *2211*, 012006. [[CrossRef](#)]
4. Visser, S.; Filatov, M.; Schreiner, P.; Shaik, S. A REKS assessment of the face-diagonal bond in 1,3-didehydrocubane and a comparison with benzyne biradicals. *Eur. J. Org. Chem.* **2003**, *2003*, 4199–4204. [[CrossRef](#)]
5. Eaton, P.E.; Cole, T.W., Jr. The cubane system. *J. Am. Chem. Soc.* **1964**, *86*, 962–964. [[CrossRef](#)]
6. Maslov, M.M.; Lobanov, D.A.; Podlivaev, A.I.; Openov, L.A. Thermal stability of cubane C₈H₈. *Phys. Solid State* **2009**, *51*, 645–648. [[CrossRef](#)]
7. Sharapa, D.; Hirsch, A.; Meyer, B.; Clark, T. Cubic C₈: An observable allotrope of carbon? *ChemPhysChem* **2015**, *16*, 2165. [[CrossRef](#)]
8. Barbosa, L.S.; Moreira, E.; Lopes, A.R.; Fonseca, A.L.A.; Azevedo, D.L. Cubane and cubanoid: Structural, optoelectronic and thermodynamic properties from DFT and TD-DFT method. *J. Mol. Graph. Model.* **2021**, *103*, 107820. [[CrossRef](#)]
9. Chaban, V.V.; Prezhdo, O.V. Energy storage in cubane derivatives and their real-time decomposition: Computational molecular dynamics and thermodynamics. *ACS Energy Lett.* **2016**, *1*, 189–194. [[CrossRef](#)]
10. Houston, S.D.; Fahrenhorst-Jones, T.; Xing, H.; Chalmers, B.A.; Sykes, M.L.; Stok, J.E.; Soto, C.F.; Burns, J.M.; Bernhardt, P.V.; De Voss, J.J.; et al. The cubane paradigm in bioactive molecule discovery: Further scope, limitations and the cyclooctatetraene complement. *Org. Biomol. Chem.* **2019**, *17*, 6790–6798. [[CrossRef](#)]
11. Gopalsamy, K.; Subramanian, V. Hydrogen storage capacity of alkali and alkaline earth metal ions doped carbon based materials: A DFT study. *Int. J. Hydrogen Energy* **2014**, *39*, 2549–2559. [[CrossRef](#)]
12. Yildirim, T.; Gülseren, O.; Ciraci, S. Exohydrogenated single-wall carbon nanotubes. *Phys. Rev. B* **2001**, *64*, 075404. [[CrossRef](#)]
13. Macreadie, L.K.; Babarao, R.; Setter, C.J.; Lee, S.J.; Qazvini, O.T.; Seeber, A.J.; Tsanaktsidis, J.; Telfer, S.G.; Batten, S.R.; Hill, M.R. Enhancing multicomponent metal-organic frameworks for low pressure liquid organic hydrogen carrier separations. *Angew. Chem. Int. Edit.* **2020**, *59*, 6090–6098. [[CrossRef](#)] [[PubMed](#)]
14. Herrera, B.; Valencia, F.; Romero, A.H.; Kiwi, M.; Ramírez, R.; Toro-Labbé, A. Cubane oligomers: A density functional theory study. *J. Mol. Struct. THEOCHEM* **2006**, *769*, 183–187. [[CrossRef](#)]
15. Pichierri, F. Cubane oligomers: Substituent effects in cubane and hypercubane: A DFT and QTAIM study. *Theor. Chem. Acc.* **2017**, *136*, 114. [[CrossRef](#)]
16. Chaglayan, B.; Huran, A.W.; Ben Amor, N.; Brumas, V.; Evangelisti, S.; Leininger, T. Cubane oligomers: Spherical aromaticity and electron delocalization in C₈ and B₄N₄ cubic systems. *Theor. Chem. Acc.* **2018**, *138*, 5. [[CrossRef](#)]
17. Katin, K.P.; Maslov, M.M. Chemical functionalization effects on cubane-based chain electronic transport. *Adv. Cond. Mat. Phys.* **2015**, *2015*, 754873. [[CrossRef](#)]
18. Katin, K.P.; Maslov, M.M. Toward CL-20 crystalline covalent solids: On the dependence of energy and electronic properties on the effective size of CL-20 chains. *J. Phys. Chem. Solids* **2017**, *108*, 82–87. [[CrossRef](#)]
19. Khorobrykh, F.; Kulnitskiy, B.; Churkin, V.; Skryleva, E.; Parkhomenko, Y.; Zholudev, S.; Blank, V.; Popov, M. The effect of C₆₀ fullerene polymerization processes on the mechanical properties of clusters forming ultrahard structures of 3D C₆₀ polymers. *Diam. Relat. Mater.* **2022**, *124*, 108911. [[CrossRef](#)]
20. Savin, A.V.; Kivshar, Y.S. Anomalous thermal relaxation in carbon nanoclusters. *Appl. Phys. Lett.* **2011**, *98*, 193106. [[CrossRef](#)]
21. Wang, J.; Gao, Q.; Gao, Y.; Luo, Y.; Guo, J.; Sun, Q.; Liang, E. Uniaxial negative thermal expansion behavior of β-CuSCN. *Appl. Phys. Lett.* **2021**, *118*, 222105. [[CrossRef](#)]
22. Koocher, N.Z.; Huang, L.-F.; Rondinelli, J.M. Negative thermal expansion in the Ruddlesden-Popper calcium titanates. *Phys. Rev. Mater.* **2021**, *5*, 053601. [[CrossRef](#)]
23. D'Ambrumenil, S.; Zbiri, M.; Chippindale, A.M.; Hibble, S.J.; Marelli, E.; Hannon, A.C. Lattice dynamics and negative thermal expansion in the framework compound ZnNi(CN)₄ with two-dimensional and three-dimensional local environments. *Phys. Rev. B* **2019**, *99*, 024309. [[CrossRef](#)]
24. Campbell, B.; Howard, C.J.; Averett, T.B.; Whittle, T.A.; Schmid, S.; Machlus, S.; Yost, C.; Stokes, H.T. An algebraic approach to cooperative rotations in networks of interconnected rigid units. *Acta Crystallogr. A* **2018**, *74*, 408. [[CrossRef](#)]

25. Dove, M.T.; Du, J.; Wei, Z.; Keen, D.A.; Tucker, M.G.; Phillips, A.E. Quantitative understanding of negative thermal expansion in scandium trifluoride from neutron total scattering measurements. *Phys. Rev. B* **2020**, *102*, 094105. [[CrossRef](#)]
26. Pavlov, I.S.; Erofeev, V.I.; Muravieva, A.V.; Vasiliev, A.A. On estimation of the rotational wave velocity in a simple cubic lattice of a fullerite crystal. *Bull. Russ. Acad. Sci. Phys.* **2021**, *85*, 686–690. [[CrossRef](#)]
27. Savin, A.V.; Kivshar, Y.S. Nonlinear breatherlike localized modes in C₆₀ nanocrystals. *Phys. Rev. B* **2012**, *85*, 125427. [[CrossRef](#)]
28. Bubenchikov, A.M.; Bubenchikov, M.A.; Lun-Fu, A.V.; Ovchinnikov, V.A. Gyroscopic effects in fullerite crystal upon deformation. *Eur. Phys. J. Plus* **2021**, *136*, 388. [[CrossRef](#)]
29. Bubenchikov, A.M.; Bubenchikov, M.A.; Lun-Fu, A.V.; Ovchinnikov, V. A. Rotational dynamics of fullerenes in the molecular crystal of fullerite. *Phys. Status Solidi A* **2021**, *218*, 2000174. [[CrossRef](#)]
30. Bubenchikov, A.; Bubenchikov, M.; Mamontov, D. The dynamic state of a pseudo-crystalline structure of B₄₂ molecules. *Crystals* **2020**, *10*, 510. [[CrossRef](#)]
31. Savin, A.V.; Dmitriev, S.V. The frequency spectrum of rotobreathers with many degrees of freedom. *Europhys. Lett.* **2022**, *137*, 36005. [[CrossRef](#)]
32. Dmitriev, S.V.; Sunagatova, I.R.; Ilgamov, M.A.; Pavlov, I.S. Natural frequencies of bending vibrations of carbon nanotubes. *Tech. Phys.* **2022**, *67*, 7–13. [[CrossRef](#)]
33. Savin, A.V.; Korznikova, E.A.; Dmitriev, S.V. Plane vibrational modes and localized nonlinear excitations in carbon nanotube bundle. *J. Sound Vib.* **2022**, *520*, 116627. [[CrossRef](#)]
34. Savin, A.V.; Sunagatova, I.R.; Dmitriev, S.V. Rotobreathers in a chain of coupled elastic rotators. *Phys. Rev. E* **2021**, *104*, 034207. [[CrossRef](#)]
35. Dmitriev, S.; Semenov, A.; Savin, A.; Ilgamov, M.; Bachurin, D.V. Rotobreather in a carbon nanotube bundle. *J. Micromechanics Mol. Phys.* **2020**, *2020*, 2050010. [[CrossRef](#)]
36. Kuzkin, V.A.; Krivtsov, A.M. Description for mechanical properties of graphene using particles with rotational degrees of freedom. *Dokl. Phys.* **2011**, *56*, 527–530. [[CrossRef](#)]
37. Berinskii, I.; Kuzkin, V.A. Equilibration of energies in a two-dimensional harmonic graphene lattice. *Philos. T. R. Soc. A* **2020**, *378*, 20190114. [[CrossRef](#)]
38. Dudek, K.K.; Attard, D.; Caruana-Gauci, R.; Wojciechowski, K.W.; Grima, J.N. Unimode metamaterials exhibiting negative linear compressibility and negative thermal expansion. *Smart Mater. Struct.* **2016**, *25*, 025009. [[CrossRef](#)]
39. Dudek, K.K.; Gatt, R.; Mizzi, L.; Dudek, M.R.; Attard, D.; Evans, K.E.; Grima, J.N. On the dynamics and control of mechanical properties of hierarchical rotating rigid unit auxetics. *Sci. Rep.* **2017**, *7*, 46529. [[CrossRef](#)]
40. Gatt, R.; Mizzi, L.; Azzopardi, J.L.; Azzopardi, K.M.; Attard, D.; Casha, A.; Briffa, J.; Grima, J.N. Hierarchical auxetic mechanical metamaterials. *Sci. Rep.* **2015**, *5*, 8395. [[CrossRef](#)]
41. Vasiliev, A.A.; Dmitriev, S.V.; Ishibashi, Y.; Shigenari, T. Elastic properties of a two-dimensional model of crystals containing particles with rotational degrees of freedom. *Phys. Rev. B* **2002**, *65*, 8395. [[CrossRef](#)]
42. Vasiliev, A.A.; Pavlov, I.S. Auxetic properties of chiral hexagonal Cosserat lattices composed of finite-sized particles. *Phys. Status Solidi B* **2020**, *257*, 1900389. [[CrossRef](#)]
43. Jamari, J.; Ammarullah, M.I.; Santoso, G.; Sugiharto, S.; Supriyono, T.; Prakoso, A.T.; Basri, H.; van der Heide, E. Computational Contact Pressure Prediction of CoCrMo, SS 316L and Ti₆Al₄V Femoral Head against UHMWPE Acetabular Cup under Gait Cycle. *J. Funct. Biomater.* **2022**, *13*, 64. [[CrossRef](#)] [[PubMed](#)]
44. Li, B.; Zhang, J.; Yan, Z.; Feng, M.; Yu, Z.; Wang, L. Pressure-induced dimerization of C₆₀ at room temperature as revealed by an in situ spectroscopy study using an infrared laser. *Crystals* **2020**, *10*, 182. [[CrossRef](#)]
45. Meletov, K.P.; Christofilos, D.; Kourouklis, G.A.; Ves, S. Pressure induced phase transitions in C₆₀ single crystals. *Chem. Phys. Lett.* **1995**, *236*, 265–270. [[CrossRef](#)]
46. Quo, Y.; Karasawa, N.; Goddard, W.A., III. Prediction of fullerene packing in C₆₀ and C₇₀ crystals. *Nature* **1991**, *351*, 464–467. [[CrossRef](#)]
47. Bortel, G.; Kováts, E.; Földes, D.; Jakab, E.; Durkó, G.; Pekker, S. Recognition-control and host-guest interactions in high-symmetry cocrystals of fullerenes with cubane and mesitylene. *Cryst. Growth Des.* **2020**, *20*, 4169–4175. [[CrossRef](#)]
48. Savin, A.V.; Kivshar, Y.S.; Hu, B. Suppression of thermal conductivity in graphene nanoribbons with rough edges. *Phys. Rev. B* **2010**, *82*, 195422. [[CrossRef](#)]
49. Savin, A.V.; Korznikova, E.A.; Dmitriev, S.V. Dynamics of surface graphene ripplocations on a flat graphite substrate. *Phys. Rev. B* **2019**, *99*, 235411. [[CrossRef](#)]
50. Brenner, D.W. Empirical potential for hydrocarbons for use in simulating the chemical vapor deposition of diamond films. *Phys. Rev. B* **1990**, *42*, 9458–9471. [[CrossRef](#)]
51. Brenner, D.W.; Shenderova, O.A.; Harrison, J.A.; Stuart, S.J.; Ni, B.; Sinnott, S.B. A second-generation reactive empirical bond order (REBO) potential energy expression for hydrocarbons. *J. Phys. Condens. Matter* **2002**, *14*, 783–802. [[CrossRef](#)]
52. Marks, N.A. Generalizing the environment-dependent interaction potential for carbon. *Phys. Rev. B* **2000**, *63*, 035401. [[CrossRef](#)]
53. Tersoff, J. Empirical interatomic potential for carbon, with applications to amorphous carbon. *Phys. Rev. Lett.* **1988**, *61*, 2879–2882. [[CrossRef](#)] [[PubMed](#)]
54. Los, J.H.; Fasolino, A. Intrinsic long-range bond-order potential for carbon: Performance in Monte Carlo simulations of graphitization. *Phys. Rev. B* **2003**, *68*, 24107. [[CrossRef](#)]

55. Srinivasan, S.G.; van Duin, A.C.T.; Ganesh, P. Development of a ReaxFF potential for carbon condensed phases and its application to the thermal fragmentation of a large fullerene. *J. Phys. Chem.* **2015**, *119*, 571–580. [[CrossRef](#)] [[PubMed](#)]
56. Stuart, S.J.; Tutein, A.B.; Harrison, J.A. A reactive potential for hydrocarbons with intermolecular interactions. *J. Chem. Phys.* **2000**, *112*, 6472–6486. [[CrossRef](#)]
57. Rowe, P.; Deringer, V.L.; Gasparotto, P.; Csányi, G.; Michaelides, A. An accurate and transferable machine learning potential for carbon. *J. Chem. Phys.* **2020**, *153*, 10897690. [[CrossRef](#)]
58. Babicheva, R.I.; Semenov, A.S.; Shcherbinin, S.A.; Korznikova, E.A.; Kudreyko, A.A.; Vivegananthan, P.; Zhou, K.; Dmitriev, S.V. Effect of the stiffness of interparticle bonds on properties of delocalized nonlinear vibrational modes in an fcc lattice. *Phys. Rev. E* **2022**, *105*, 064204. [[CrossRef](#)]
59. Goldstein, R.V.; Gorodtsov, V.A.; Lisovenko, D.S. Classification of cubic auxetics. *Phys. Status Solidi B* **2013**, *250*, 2038–2043. [[CrossRef](#)]
60. Epishin, A.I.; Lisovenko, D.S. Extreme values of the Poisson's ratio of cubic crystals. *Tech. Phys.* **2016**, *61*, 1516–1524. [[CrossRef](#)]
61. Goldstein, R.V.; Gorodtsov, V.A.; Lisovenko, D.S. Cubic auxetics. *Dokl. Phys.* **2011**, *56*, 399–402. [[CrossRef](#)]
62. Lisovenko, D.S.; Baimova, J.A.; Rysaeva, L.K.; Gorodtsov, V.A.; Rudskoy, A.I.; Dmitriev, S.V. Equilibrium diamond-like carbon nanostructures with cubic anisotropy: Elastic properties. *Phys. Status Solidi B* **2016**, *253*, 1295–1302. [[CrossRef](#)]
63. Zarochentsev, E.V.; Troitskaya, E.P.; Chabanenko, V.V. Elastic constants of noble-gas crystals under pressure and the Cauchy relations. *Phys. Solid State* **2004**, *46*, 249. [[CrossRef](#)]
64. Hoen, S.; Chopra, N.G.; Xiang, X.-D.; Mostovoy, R.; Hou, J.; Vareka, W.A.; Zettl, A. Elastic properties of a van der Waals solid: C₆₀. *Phys. Rev. B* **1992**, *46*, 12737. [[CrossRef](#)]
65. Funamori, Y.; Suzuki, R.; Wakahara, T.; Ohmura, T.; Nakagawa, E.; Tachibana, M. Large elastic deformation of C₆₀ nanowhiskers. *Carbon* **2020**, *169*, 65–72. [[CrossRef](#)]
66. Asaka, K.; Kato, R.; Miyazawa, K.; Kizuka, T. Buckling of C₆₀ whiskers. *Appl. Phys. Lett.* **2006**, *89*, 071912. [[CrossRef](#)]
67. Shepelev, I.A.; Bachurin, D.V.; Korznikova, E.A.; Dmitriev, S.V. Highly efficient energy and mass transfer in bcc metals by supersonic 2-crowdions. *J. Nucl. Mater.* **2022**, *568*, 153841. [[CrossRef](#)]
68. Prokhorov, V.M.; Blank, V.D.; Dubitsky, G.A.; Berezina, S.; Levin, V.M. Elastic and microstructural properties of C₆₀- and C₇₀-based polymerized fullerites exposed to high pressure (15 GPa) and elevated temperatures. *J. Phys. Condens. Mat.* **2002**, *14*, 11305–11310. [[CrossRef](#)]